ROYAL SOCIETY OF CHEMISTRY View Article Online
DOI: 10.1039/D1CC01578H

Journal Name

COMMUNICATION

High-Efficient Electrocatalyst for Overall Water Splitting: Mesoporous CoS/MoS_2 with Hetero-Interface

Wen-Huan Huang,[ab] *Xi-Ming Li,*[a] *Xiu-Fang Yang,*[a] *Hua-Bin Zhang,*[c] *Fei Wang,*[b] *and Jian Zhang,*[*b]

Received 00th January 20xx,
Accepted 00th January 20xx

DOI: 10.1039/x0xx00000x

www.rsc.org/

A mesoporous CoS/MoS_2 with abundant heterogeneous interfaces was facile synthesized from bimetallic hybrid zeolitic imidazolate framework, which showed excellent catalytic activity and reaction kinetics on both HER and OER in 1 M KOH. Meanwhile, as cathode and anode in water splitting electrocatalysis, it delivers a low cell voltage of 1.61 V at 10 mA cm^{-2} and brilliant durability.

Electrochemical water splitting to obtaining hydrogen as clean energy is of significance for solving the energy crisis and environmental problems.[1-3] The key for realizing high-efficient water electrolysis is the assembly of brilliant electrocatalysts for oxygen evolution reaction (OER) and the hydrogen evolution reaction (HER).[4-6] At present, Pt-based and Ir/Ru-based materials are considered as most efficient electrocatalysts for the HER and OER, respectively, but their large-scale applications are restricted by the high-price of noble metals.[7-10] As consequence, many excellent transition-metal-based electrocatalyst, such as carbides, oxides, phosphides, nitrides, and sulfides, have been synthesized by scientists which showed excellent electrocatalytic performance with different structural and catalytic characters.[11-14]

Among them, transition metal sulfides, such as MoS_2 and CoS based hybrids have been widely studied as HER and OER electrocatalysts for their low cost and high activity.[15-18] Recently, some binary sulfides have been assembled as bifunctional electrocatalyst and applied in symmetric electrode electrolyzer, showing excellent catalytic activities.[19-21] For example, Gao et al. reported a MoS_2/Ni_3S_2 hetero-nanorod as cathode and anode were applied in electrocatalytic water splitting.[22] The distinct synergistic and electron-coupling effect between Co and Ni achieved low potential and excellent durability. The interfacial designed of binary composite is the key for improving the catalytic performance, including the kinds, number, and distribution of catalytic centers.[23-26]

However, the accurate synthesizing the binary sulfides with numerous heterogeneous interfaces and exposed catalytic atoms is still challenging. Herein, a CoMo-bimetallic Hybrid zeolitic imidazolate framework (HZIF) is employed as precursor, which is orderly crystallized form Co^{2+}, imidazole, and MoO_4 in a specific ratio of 4:6:1 through the im-M-O-T connections[27-31], and *in-situ* converted into mesoporous CoS/MoS_2 through one-step facile sulfidation (Fig. S1). The mesopores in binary sulfide provide abundant accessible hetero-interfaces and exposed active sites, which greatly promote the catalytic activity and accelerate the charge and mass transfer processes. As expect, excellent electrocatalytic HER and OER performances and outstanding stabilities of CoS/MoS_2 in alkaline media were observed. Furthermore, as symmetric electrodes in water electrolyzer, it exhibited a low cell voltage of 1.61 V at the current density of 10 mA cm^{-2}, comparabled with the commercial RuO_2||Pt/C and best reported transition metal-based electrocatalysts.[32]

The HZIF-1-CoMo, as the precursor, was synthesized through a typical procedure and its PXRD peaks are evaluated by comparing with simulated XRD result (Fig. S2). Then, HZIF-1-CoMo powder was refluxed with thioacetamide (TAA) at 90 °C for 1 h and *in-situ* transformed into binary sulfide composite (CoS/MoS_2). The structural information of CoS/MoS_2 were characterized and investigated by TGA, PXRD, Raman and BET results, which were shown in Fig. S3-S4. The characteristic peaks in XRD curve of CoS/MoS_2 are well-consistent with those in the standard CoS (PDF 25-1081) and MoS_2 (PDF 37-1492) curves (Fig. S4a). The peaks in 30.5°, 35.3° and 46.7° are corresponding to the (100), (101) and (102) plane of CoS, while the peaks in 29.0°, 33.5°, 35.8° and 39.5° are assigned to (004), (101), (102) and (103) plane of MoS_2. Raman spectrum of CoS/MoS_2 shows two dominant peaks at 382 and 410 cm^{-1}, corresponding to the in-plane of E^1_{2g} and out plane of A_{1g} vibrational modes of MoS_2.

[a] *Key Laboratory of Chemical Additives for China National Light Industry, College of Chemistry and Chemical Engineering, Shaanxi University of Science and Technology, 710021, Xi'an, China. E-mail: huangwenhuan@sust.edu.cn*
[b] *State Key Laboratory of Structural Chemistry, Fujian Institute of Research on the Structure of Matter, Chinese Academy of Sciences, 350002, Fuzhou, China*
[c] *KAUST Catalysis Center, King Abdullah University of Science and Technology, 23955-6900, Thuwal, Kingdom of Saudi Arabia.*
Electronic Supplementary Information (ESI) available: experimental details and analysis. DOI: 10.1039/x0xx00000x

The peak at 281 cm^{-1} is assigned to the liberation (E_g) band of cubic CoS (Fig. S4b).[33, 34] These results confirmed the chemical component of the CoS/MoS_2 and the fully in-situ transform of the HZIF-CoMo.

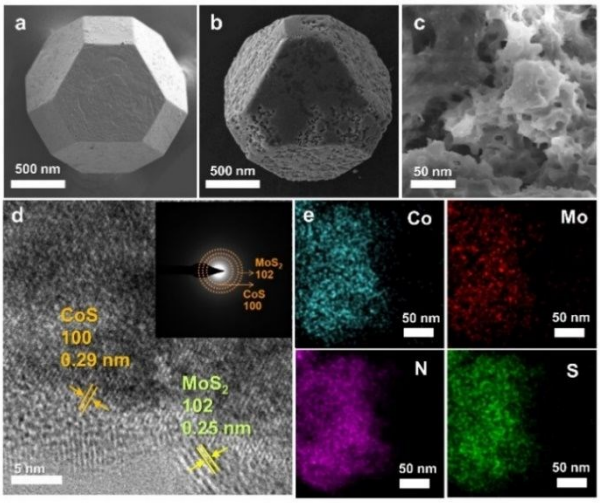

Fig. 1. SEM of HZIF-1-CoMo (a) and CoS/MoS_2 (b)-(c), TEM and SAED of CoS/MoS_2 (d), and EDS mapping of CoS/MoS_2 (e).

For investigating the morphology of the CoS/MoS_2, The SEM of both HZIF-1-CoMo and CoS/MoS_2 were conducted. The Fig. 1a shows a well-defined truncated octahedron for crystalline HZIF-CoMo with the particle size of about 2 µm. As shown in Fig.1b-1c, CoS/MoS_2 maintains the same morphology with HZIF-1-CoMo after the sulfidation, but with rough surfaces and abundant internal mesopores. The mesoporous structure was further confirmed by BET results (Fig. S4c-d) which showed a high specific surface area of 440.5 m^2/g and abundant pores with the diameter of 4-5 nm. The mesoporous structure of the binary sulfide is greatly benefit for exposing more accessible heterointerface and the conducting charge and reaction species. Then, the TEM and EDS was performed to study the internal structure of the HZIF-CoMo derived CoS/MoS_2 binary (Fig. 1d-e). The inter-planar spacings of 0.25 and 0.29 nm in Fig.1d are attributed to the (100) and (102) planes of CoS and MoS_2, respectively, which are in accordance with the diffraction rings in SAED image and PXRD result. The EDS mapping displayed the highly uniform distribution of Co, Mo, S, and N elements in the CoS/MoS_2. These results revealed that the excellent fully incorporated structure of CoS and MoS_2 in the CoS/MoS_2, which will bring strong electronic coupling through the Mo and Co atoms.

This speculation was further confirmed by XPS results as shown in Fig. 2. The valent state, charge transfer and coupling interaction on the surface of CoS/MoS_2 was studied by contrast with those of pure MoS_2 and CoS (Fig. 2). The XPS spectra of Co 2p for CoS/MoS_2 and pure CoS (Fig. 2b) revealed the coexistence of Co^{2+} and Co^{3+}. The binding energies at ~795.74 eV and ~779.60 eV correspond to Co^{3+} $2p_{1/2}$ and Co^{3+} $2p_{3/2}$, and the binding energies at ~801.20 eV and ~784.30 eV are attributable to Co^{2+} $2p_{1/2}$ and Co^{2+} $2p_{3/2}$, respectively. The negative shifts of Co 2p for CoS/MoS_2 comparing with the pure CoS is observed which is due to the electronic coupling and charge transfer between CoS and MoS_2 in the hybrid. The Mo 3d spectra of CoS/MoS_2 (Fig. 2c) displayed two pronounced peaks at about 233.40 and 230.2 eV which are assigned to Mo $3d_{3/2}$ and Mo $3d_{5/2}$ of Mo^{4+}. As comparison with pure MoS_2, the distinct positive shifts of CoS/MoS_2 also indicated the electronic regulation between Co and Mo. The S 2p XPS spectra of CoS/MoS_2 composite and pure CoS and MoS_2 are conducted (Fig. 2d). The 161.7 and 162.1 eV peaks are corresponding to the S $2p_{3/2}$ and S $2p_{1/2}$, which consistent with those reported sulfides.

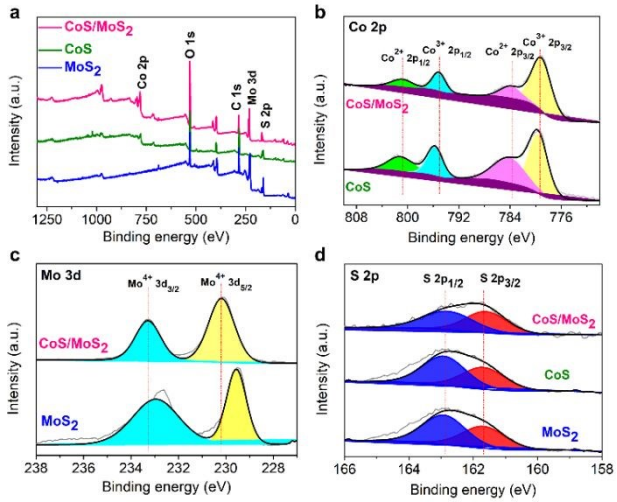

Fig. 2. XPS spectra (a) of CoS, MoS_2 and CoS/MoS_2, and XPS of Co 2p (b), Mo 3d (c), and S 2p (d).

The electrochemical performance of the CoS/MoS_2 toward the OER was first evaluated in O_2-saturated 1.0 M KOH based on a typical three electrode system. For comparison, CoS, MoS_2 and commercial RuO_2 were evaluated at the same conditions. The LSV curves of all catalysts are shown in Fig. 3a. As expected, the CoS/MoS_2 shows best catalytic activity towards OER. The overpotential of 281 mV for CoS/MoS_2 to reaching the current density of 10 mA cm^{-2} is much lower than those for CoS (340 mV), MoS_2 (434 mV) and RuO_2 (314 mV). In the hybrid, the synergetic effect between CoS and MoS_2 on the heterogenous interface greatly enhanced the catalytic activity. Additionally, the Tafel slopes were fitted for studying the OER kinetics of the catalysts (Fig. 3b). The CoS/MoS_2 showed the smallest Tafel slope of 79 mV dec^{-1}, comparing with those of CoS (128 mV dec^{-1}), MoS_2 (141 mV dec^{-1}) and RuO_2 (118 mV dec^{-1}). The abundant mesopores in the hybrid are contributed to the fast mass transfer in the OER process.

The electrochemical impedance (EIS) curves are fitted to study the charge transfer of the catalysts (Fig. S5). The CoS/MoS_2 composite exhibited a smaller charge-transfer resistance (R_{ct}) of 41 Ω than those of CoS (111 Ω), MoS_2 (120 Ω) and RuO_2 (89 Ω, which indicated that the ultrafine nanostructures, high surface areas and the electronic coupling between Co and Mo in the binary sulfides greatly enhanced the charge transfer in the OER process. Furthermore, the electrochemically active surface area (ECSA) of the catalysts

were evaluated by C_{dl} values. As shown in Fig. 3c, the calculated C_{dl} of CoS/MoS_2 is 87 mF cm^2, which is larger than those of CoS (7 mF cm^2), MoS_2 (5 mF cm^2) and RuO_2 (14 mF cm^2). The relatively high C_{dl} value implied that the CoS/MoS_2 expose more active sites, thus improving the catalytic activity. It owning to the highly porous structure of CoS/MoS_2, which provide more accessible active sites on the interface. As another vital factor, electrocatalytic durability of CoS/MoS_2 was investigated through the continuous CV scan and chronoamperometry measurement. As shown in Fig. 3d, after continuously CV scans for 1000 cycles at a scanning rate of 2 mV/S, the LSV curve of CoS/MoS_2 showed a slight positive shift at the current density of 10 mA cm^{-2}. The chronoamperometry measurement of CoS/MoS_2 was performed at the current density of 10 mA cm^{-2} for 12 h. The stable i-t curve also conformed the excellent stability of the CoS/MoS_2.

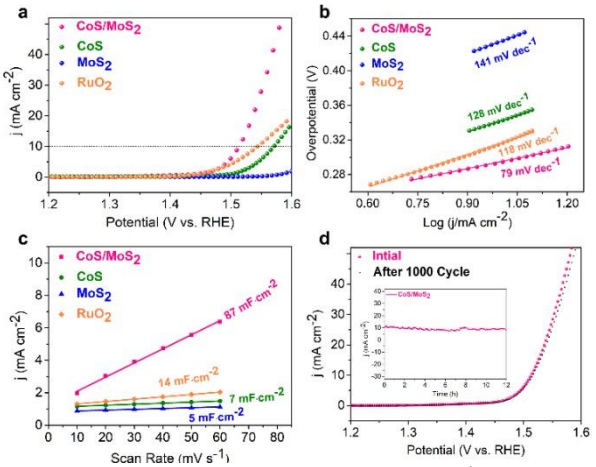

Fig. 3. LSV curves (a), Tafel plots (b), and C_{dl} (c) of CoS/MoS_2, CoS, MoS_2 and RuO_2 for OER electrocatalysis in 1M KOH, LSV curves for CoS/MoS_2 before and after 1000 cycles of CV scanning (d) and i-t curve of CoS/MoS_2 for 12 hours (insert in d).

Furthermore, the electrocatalytic HER performance of the CoS/MoS_2 catalyst was also investigated in 1M KOH. The catalytic performance of CoS, MoS_2 and commercial Pt/C (20 wt%) were performed for comparison. As a result, the LSV curves in Fig. 4a displayed the smallest overpotential of 180 mV for CoS/MoS_2 to reaching the current density of 10 mA cm^{-2}, which is far beyond the CoS (456 mV) and MoS_2 (503 mV) in M KOH. The corresponding Tafel slope of the CoS/MoS_2 is 72 mV·dec^{-1}, which is also smaller than those of CoS (206 mV·dec^{-1}) and MoS_2 (277 mV·dec^{-1}) (Fig. 4b). Comparing with the CoS and MoS_2, the lower R_{ct} of 63 Ω and higher C_{dl} of 35.1 mF cm^2 for CoS/MoS_2 were observed in Fig. 4c and S6, which indicated the fast charge transfer and the high amount of exposed active sites for serving as HER electrocatalyst. The durability of the CoS/MoS_2 in HER process was also evaluated, which showed a high-performed LSV curve after the 1000 cycles CV scanning and a stable 12-hour i-t curve (Fig.4d).

As summarized in Tables S3, the brilliant OER and HER catalytic performance of CoS/MoS_2 indicated that it might further be employed as bifunctional electrocatalyst in a water electrolyzer. Therefore, the CoS/MoS_2 was loaded on two pieces of nickel foam (NF) with the loading amount of 2 mg cm^{-2} were employed as both cathode and anode in the water splitting process. The electrocatalytic performance of $CoS/MoS_2||CoS/MoS_2$ was evaluated in 1 M KOH through the LSV curve at the scanning rate of 2 mV s^{-1}, comparing with the naked NF||NF.

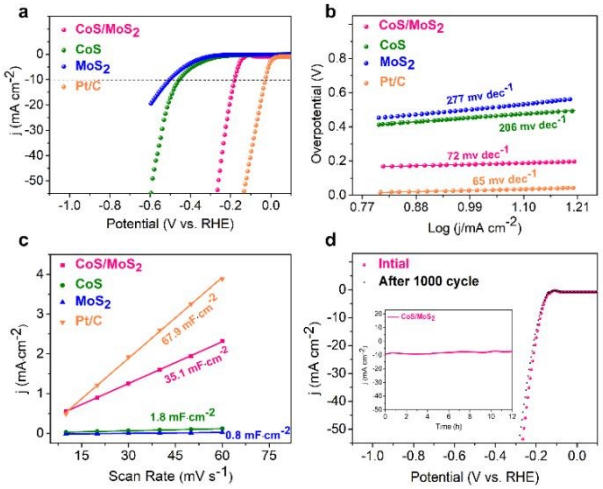

Fig. 4. LSV curves (a), Tafel plots (b), and C_{dl} (c) of CoS/MoS_2, CoS, MoS_2 and Pt/C (20 wt%) for HER electrocatalysis in 1M KOH, LSV curves of CoS/MoS_2 before and after 1000 cycles of CV scanning (d) and i-t curve of CoS/MoS_2 for 12 hours (insert in d).

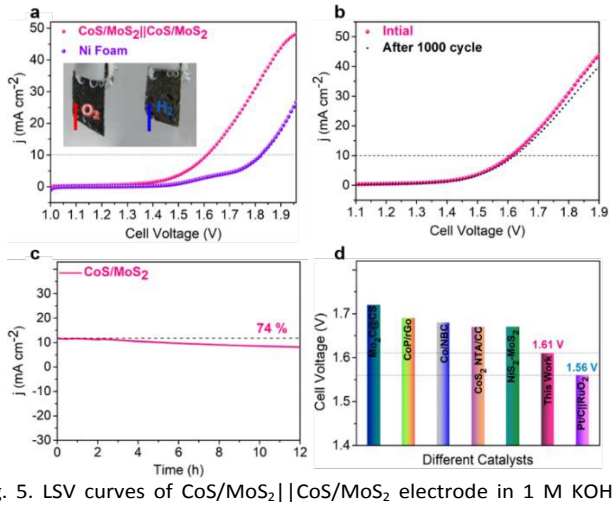

Fig. 5. LSV curves of $CoS/MoS_2||CoS/MoS_2$ electrode in 1 M KOH at scanning rate of 2 mV·s^{-1} (a) and digital photograph of the evolution of H_2 and O_2 gas from the electrodes during electrolysis (inset), LSV curves before and after 1000 cycles of CV scanning (b), chronoamperometry curve of $CoS/MoS_2||CoS/MoS_2$ for 12 hours (c), comparison of other reported Co or Mo based catalyst (d).

As shown in Fig. 5a, it exhibited a cell voltage of 1.61 V (corresponding to an overpotential of 380 mV) to achieve the current density of 10 mA·cm^{-2}, which is far beyond the NF||NF. Large number of bubbles were produced from both the cathode (H_2) and anode (O_2) during the water electrolysis. The overall water splitting performance of the CoS/MoS_2 catalyst is comparable with the best reported Co- or Mo-based water splitting electrocatalysts (Table S1). After 1000 cycles of CV scanning, the stable LSV curve was also observed with a small positive shift of η_{10} (Fig. 5b). The i-t curve of CoS/MoS_2 at the current of 10 mA cm^2 for 12 hours showed the relatively good

stability (current attenuation of 26%) (Fig. 5c). The above results indicates that CoS/MoS_2 is a promising candidate for serving as electrode in symmetric water electrolyzer in alkaline condition.

In summary, a mesoporous binary CoS/MoS_2 was assembled through a facile sulphuration process from a bimetallic CoMo-HZIF which exhibited excellent electrocatalytic OER, HER and superior water splitting performance. The mesopores in CoS/MoS_2 not only exposed a larger amount of accessible active sites, but also promote the charge transfer and the mass transfer at the contacting interfaces. Therefore, brilliant activity and kinetics were observed. The synergistic effect and strong interaction between Co and Mo in the composite enhanced the catalytic activities in both OER and HER processes, resulting in a well-performance in water splitting. This work presents a good example and lights the new sights for designing heterogenous interface in binary composite. Although the durability of this binary sulfide cannot meet the requirement of the practical catalysis. The excellent crystalline structure of HZIF with orderly Co-O-Mo units, employed as precursor, will provide many opportunity and possibility for constructing stable bimetallic hybrid water splitting electrocatalysts in future.

This work was financially supported by the National Natural Science Foundation of China (22001156), the open Foundation of State Key Laboratory of Structural Chemistry (20180024), the open Foundation of Key Laboratory of Coal to Ethylene Glycol and Its Related Technology (201801).

Conflicts of interest

There are no conflicts to declare.

Notes and references

1. C. P. Wang, L. J. Kong, H. Sun, M. Zhong, H. J. Cui, Y. H. Zhang, D. H. Wang, J. Zhu and X. H. Bu, ChemElectroChem, 2019, 6, 5603-5609.
2. J. H. Lin, P. C. Wang, H. H. Wang, C. Li, X. Q. Si, J. L. Qi, J. Cao, Z. X. Zhong, W. D. Fei and J. C. Feng, Advanced Science, 2019, 6, 1900246.
3. P. Zhu, A. L. Li, Z. X. Yang, Y. Zhou, X. Xiong and F. P. Ouyang, ACS Applied Energy Materials, 2019, 3, 129-134.
4. X. Zhang, S. W. Liu, Y. P. Zang, R. R. Liu, G. Q. Liu, G. Z. Wang, Y. X. Zhang, H. M. Zhang and H. J. Zhao, Nano Energy, 2016, 30, 93-102.
5. J. H. Bao, Y. M. Zhou, Y. W. Zhang, X. L. Sheng, Y. Y. Wang, S. Liang, C. Guo, W. Yang, T. Zhuang and Y. J. Hu, Journal of Materials Chemistry A, 2020, 8, 22181-22190.
6. J. G. Li, K. F. Xie, H. C. Sun, Z. S. Li, X. Ao, Z. H. Chen, K. K. Ostrikov, C. D. Wang and W. J. Zhang, ACS Appl Mater Interfaces, 2019, 11, 36649-36657.
7. Z. C. Li, Y. Xu, X. X. Ren and W. P. Wang, Journal of Materials Science, 2020, 55, 13892-13904.
8. Y. Yang, H. Yao, Z. Yu, S. M. Islam, H. He, M. Yuan, Y. Yue, K. Xu, W. Hao, G. Sun, H. Li, S. Ma, P. Zapol and M. G. Kanatzidis, Journal of the American Chemical Society, 2019, 141, 10417-10430.
9. Y. K. Liu, B. Hu, S. D. Wu, M. H. Wang, Z. H. Zhang, B. B. Cui, L. H. He and M. Du, Applied Catalysis B: Environmental, 2019, 258, 117970-117972.
10. C. Z. Wang, X. D. Shao, J. Pan, J. G. Hu and X. Y. Xu, Applied Catalysis B: Environmental, 2020, 268, 118435-118459. View Article Online DOI: 10.1039/D1CC00578H
11. G. Y. Zhou, X. M. Wu, M. M. Zhao, H. Pang, L. Xu, J. Yang and Y. W. Tang, ChemSusChem, 2020, 14, 699-708.
12. N. Huang, S. F. Yan, M. Y. Zhang, Y. Y. Ding, L. Yang, P. P. Sun and X. H. Sun, Electrochimica Acta, 2019, 327, 13492-13500.
13. T. Wang, X. Zhang, P. Yang and S. P. Jiang, Inorganic Chemistry Frontiers, 2020, 7, 3578-3587.
14. Y. Q. Liu, Y. Yu, Z. C. Mu, Y. H. Wang, U. Ali, S. Y. Jing and S. X. Xing, Inorganic Chemistry Frontiers, 2020, 7, 3588-3597.
15. H. J. Xu, J. Cao, C. F. Shan, B. K. Wang, P. X. Xi, W. S. Liu and Y. Tang, Angewandte Chemie International Edition, 2018, 57, 8654-8658.
16. X. B. Hou, H. M. Zhou, M. Zhao, Y. B. Cai and Q. F. Wei, ACS Sustainable Chemistry & Engineering, 2020, 8, 5724-5733.
17. L. Yan, H. Y. Wang, J. L. Shen, J. Q. Ning, Y. J. Zhong and Y. Hu, Chemical Engineering Journal, 2021, 403, 126385.
18. C. Y. Li, M. D. Liu, H. Y. Ding, L. Q. He, E. Z. Wang, B. L. Wang, S. S. Fan and K. Liu, Journal of Materials Chemistry A, 2020, 8, 17527-17536.
19. X. B. Xu, W. Zhong, L. Zhang, G. X. Liu and Y. W. Du, International Journal of Hydrogen Energy, 2020, 45, 17329-17338.
20. S. D. Guan, X. L. Fu, Z. Z. Lao, C. H. Jin and Z. J. Peng, Sustainable Energy & Fuels, 2019, 3, 2056-2066.
21. Q. Qin, L. L. Chen, T. Wei and X. Liu, Small, 2019, 15, e1803639.
22. Y. Q. Yang, K. Zhang, H. L. Lin, X. Li, H. C. Chan, L. C. Yang and Q. S. Gao, ACS Catalysis, 2017, 7, 2357-2366.
23. V. Ganesan and J. Kim, Int. J. Hydrogen Energy, 2020, 45, 13290-13299.
24. L. H. He, S. J. Huang, Y. K. Liu, M. H. Wang, B. B. Cui, S. D. Wu, J. M. Liu, Z. H. Zhang and M. Du, Journal of Colloid and Interface Science, 2020, 586, 538-550.
25. S. P. Lonkar, V. V. Pillai and S. M. Alhassan, Materials Advances, 2020, 1, 794-803.
26. L. C. Huang, L. S. Xu, Y. Yang, H. Yu, H. Y. Tao, D. Li and X. T. Dong, Journal of Materials Science: Materials in Electronics, 2020, 31, 6607-6617.
27. F. Wang, Z. S. Liu, H. Yang, Y. X. Tan and J. Zhang, Angewandte Chemie International Edition, 2011, 50, 450-453.
28. W. H. Huang, X. M. Li, D. Y. Yu, X. F. Yang, L. F. Wang, P. B. Liu and J. Zhang, Nanoscale, 2020, DOI: 10.1039/d0nr04418k.
29. W. H. Huang, X. X. Zhang, Y. N. Zhao, J. Zhang and P. B. Liu, Carbon, 2020, 167, 19-30.
30. Y. Li, R. P. Zhang, W. Zhou, X. Wu, H. B. Zhang and J. Zhang, ACS Nano, 2019, 13, 5533-5540.
31. W.-H. Huang, X.-M. Li, X.-F. Yang, H.-Y. Zhang, P.-B. Liu, Y.-M. Ma and X. Lu, Chemical Engineering Journal, 2020, DOI: 10.1016/j.cej.2020.127595.
32. Z. Yu, Y. Bai, S. M. Zhang, Y. X. Liu, N. Q. Zhang and K. N. Sun, Journal of Materials Chemistry A, 2018, 6, 10441-10446.
33. V. Ganesan and J. Kim, International Journal of Hydrogen Energy, 2020, 45, 13290-13299.
34. V. Ganesan, S. Lim and J. Kim, Chem. - Asian J., 2018, 13, 413-420.